

Effect of Mg doping on morphology, photocatalytic activity and related biological properties of $Zn_{1-x}Mg_xO$ nanoparticles

Bestenur YALÇIN^{1,*}, Doğan AKCAN², İbrahim Ertuğrul YALÇIN³,
Mehmet Can ALPHAN⁴, Kenan ŞENTÜRK⁵, İbrahim İlker ÖZYİĞİT^{6,7}, Lütfi ARDA⁸

¹Department of Medical Laboratory Techniques, Vocational School of Health Services,
Bahçeşehir University İstanbul, Turkey

²Department of Mathematics Engineering, Faculty of Engineering and Natural Sciences,
Bahçeşehir University, İstanbul, Turkey

³Department of Civil Engineering, Faculty of Engineering and Natural Sciences,
Bahçeşehir University, İstanbul, Turkey

⁴Department of Electric Electronic Engineering, Faculty of Engineering and Natural Sciences,
Bahçeşehir University, İstanbul, Turkey

⁵Department of Mechatronics Engineering, Faculty of Engineering and Architecture,
İstanbul Gelişim University, İstanbul, Turkey

⁶Department of Biology, Faculty of Science and Arts, Marmara University, İstanbul, Turkey

⁷Department of Biology, Faculty of Science, Kyrgyz-Turkish Manas University, Bishkek, Kyrgyzstan

⁸Department of Mechatronics Engineering, Faculty of Engineering and Natural Sciences,
Bahçeşehir University, İstanbul, Turkey

Received: 05.04.2020

Accepted/Published Online: 26.06.2020

Final Version: 18.08.2020

Abstract: The objective of this study is to synthesize ZnO and Mg doped ZnO ($Zn_{1-x}Mg_xO$) nanoparticles via the sol-gel method, and characterize their structures and to investigate their biological properties such as antibacterial activity and hemolytic potential. Nanoparticles (NPs) were synthesized by the sol-gel method using zinc acetate dihydrate ($Zn(CH_3COO)_2 \cdot 2H_2O$) and magnesium acetate tetrahydrate ($Mg(CH_3COO)_2 \cdot 4H_2O$) as precursors. Methanol and monoethanolamine were used as solvent and sol stabilizer, respectively. Structural and morphological characterizations of $Zn_{1-x}Mg_xO$ nanoparticles were studied by using XRD and SEM-EDX, respectively. Photocatalytic activities of ZnO and selected Mg-doped ZnO ($Zn_{1-x}Mg_xO$) nanoparticles were investigated by degradation of methylene blue (MeB). Results indicated that Mg doping (both 10% and 30%) to the ZnO nanoparticles enhanced the photocatalytic activity and a little amount of $Zn_{0.90}Mg_{0.10}O$ photocatalyst (1.0 mg/mL) degraded MeB with 99% efficiency after 24 h of irradiation under ambient visible light. Antibacterial activity of nanoparticles versus *Escherichia coli* (*E. coli*) was determined by the standard plate count method. Hemolytic activities of the NPs were studied by hemolysis tests using human erythrocytes. XRD data proved that the average particle size of nanoparticles was around 30 nm. Moreover, the XRD results indicated that the patterns of Mg doped ZnO nanoparticles related to ZnO hexagonal wurtzite structure had no secondary phase for $x \leq 0.2$ concentration. For $0 \leq x \leq 0.02$, NPs showed a concentration dependent antibacterial activity against *E. coli*. While $Zn_{0.90}Mg_{0.10}O$ totally inhibited the growth of *E. coli*, upper and lower dopant concentrations did not show antibacterial activity.

Key words: Sol-gel method, Mg doped ZnO, hemolytic activity, antibacterial properties, *E. coli*

*Correspondence: bestenur.yalcin@eng.bau.edu.tr

1. Introduction

Synthesis, characterization, and application of nanoscale materials lead to the design of new functional materials and devices with unique properties. Among nanosized materials, metal-oxide nanoparticles have an incredibly big potential in many research areas due to their small particle size, large surface area and advanced chemical, optical, morphological and antibacterial properties. Metal oxide NPs can be synthesized by using biological systems as bacteria, fungi and yeast [1–4] or synthetic pathways like hydrothermal method [5,6], sol-gel method [7–11] and chemical vapor deposition [12]. Metal-oxide NPs find applications in textile industry [13,14], electronics [15,16,17], gas sensing applications [18–20], in medical applications like selective destruction of tumor cells [21], intracellular drug delivery [22] and some diagnostic applications.

Among metal-oxide NPs, zinc oxide (ZnO) has a special biological and medical importance [23–26]. ZnO NPs are regarded as biosafe due to their low toxicity in some researches [27, 28] and they are also assigned as GRAS (generally recognized as safe) by FDA (US Food and Drug Administration) [29,30]. In a related study, the effects of ZnO nanowires (average diameter of 1 μm and the average length of 200 μm) on Hela cell line (a type of epithelial cell) and L-929 cell line (connective tissue cells) were investigated by measuring the activity of succinate dehydrogenase (SDH). ZnO nanowire concentrations of 0.1, 1, 10, and 100 $\mu\text{g}/\text{mL}$ were studied, and it was stated that ZnO nanowires were completely biocompatible and biosafe at cellular level at concentrations lower than 100 $\mu\text{g}/\text{mL}$ [23]. Moreover, zinc is one of the essential elements both in plants and animals [31–33]. It has an important role in enzyme activity and acts as a cofactor of some enzymes such as carbonic anhydrase, carboxypeptidases, dipeptidases, DNA and RNA polymerases, pyruvate carboxylase and alkaline phosphatase [34,35].

Synthetic materials in contact with blood may cause damage to the walls of erythrocyte cells and may trigger various cell reactions, such as thrombus formation [36–38]. The hemolytic potential of a material is a measure of hemolysis that is caused by any material in contact with blood. ZnO NPs also show disruptive effect on biofilm formation and inhibit hemolysis so that they are assigned as hemocompatible [39]. Zhang et al. have shown that ZnO NP suspensions with 0.75 mg/ml (mg ZnO/ml physiological saline) concentration cause no apparent hemolysis [40]. Other studies on the healing of skin wounds showed that ZnO is highly effective in promoting wound healing by increasing cell reepithelization [41]. ZnO NPs are currently used in pain easing and itch relieving commercial ointments [42–44].

The antibacterial activities of metal-oxide nanoparticles are noteworthy as a new technique that can replace the traditional methods in which organic antibiotics are used. The most remarkable advantages of inorganic antimicrobial agents are being of safe and stable, as compared to their organic equivalents.

Metal-oxide nanoparticles which contain essential mineral elements like Zn, Mg and Ca (ZnO, MgO and CaO) also show antimicrobial action which their equivalent micro and macro sized materials do not possess [45–47]. In some studies, it was shown that, ZnO NPs show selective toxicity against bacteria and act as an inert nanomaterial on human cells [48–51]. Several mechanisms were introduced to the literature about the antibacterial action of ZnO NPs. In some researches, release of metal ions like Zn^{2+} from NP structure was held responsible from the antibacterial activity [52]. However, the solubility of metal oxides like ZnO is very low and concentration dependent. Besides, some researches showed that as an essential mineral, low concentrations of Zn^{2+} ion (0.01–1.00 mM) may act as a nutrient and can enhance the growth of bacteria [53]. Another accepted mechanism of antibacterial action is the electrostatic interaction between cell walls and nanoparticles and the accumulation of nanoparticles on cell membrane [54]. According to Stoimenov, the total electrical charge of

bacteria cells is negative at biological pH because of the presence of negatively charged carboxylate groups on cell wall. On the contrary, ZnO NPs are positively charged [54]. These opposite charges cause an attraction between bacteria cell and ZnO NPs which results in cell death. Pati et al. [55] have shown the disruptive effect of ZnO NPs on the integrity of bacteria cell wall and oxidative stress resistant genes in cells. ZnO NPs are known as stable at neutral or biological pH. On the contrary, in acidic media (pH 4.5), they dissolve to form Zn^{2+} ions [56]. ZnO particles accumulate on cell wall and introduce into the cell, dissolve in lysosomes having a pH range of 4.5–5.0 [57] and cause necrotic cell death [58,59]. Thus, although Zn is essential for the continuity of metabolic activities in the cell, the uncontrolled increase in Zn concentration as a result of the dissolution of ZnO nanoparticles in the cell is stated to be a reason of cell death.

Besides the other mechanisms, the main responsible effect related to the antibacterial activity of nano sized ZnO and its derivatives causing intracellular death of bacteria is the light catalyzed formation of reactive oxygen species (ROS) such as hydroxyl radical ($\cdot\text{OH}$), superoxide anion radical ($\text{O}_2^{\cdot-}$) and hydrogen peroxide (H_2O_2) [53,60–62]. ZnO nanoparticles may cause light catalyzed formation of ROS like $\text{O}_2^{\cdot-}$, $\cdot\text{OH}$ and H_2O_2 . When the concentration of ROS exceeds the defense capacity of the cell, adverse biological consequences result [63].

In this study, the effects of Mg doping ratios on morphology, photocatalytic activity and biological effects of ZnO nanoparticles were investigated. ZnO and Mg-doped $\text{ZnO}(\text{Zn}_{1-x}\text{Mg}_x\text{O})$ nanoparticles were synthesized via the sol-gel method and examined for their antibacterial activity and hemolytic potential. The effects of high doping levels (30%) of Mg on $\text{Zn}_{1-x}\text{Mg}_x\text{O}$ NPs were investigated and results were compared with pure ZnO nanoparticles.

2. Materials and methods

Zinc acetate dihydrate [$\text{Zn}(\text{CH}_3\text{COO})_2 \cdot 2\text{H}_2\text{O}$, Merck & Co., Inc., Kenilworth, NJ, USA], and magnesium acetate tetrahydrate [$\text{Mg}(\text{CH}_3\text{COO})_2 \cdot 4\text{H}_2\text{O}$, Alfa Aesar, Haverhill, MA, USA] were used as precursors without purification. HPLC grade methanol (Merck & Co., Inc.) and monoethanolamine (Merck & Co., Inc.) were used as solvent and sol stabilizer respectively. Tryptic soy agar (TSA) and tryptic soy broth (TSB) were purchased from Merck & Co., Inc. Distilled deionized water (DDW) was obtained from a Human Zeneer power 1 water purification system (Human Corporation, Seoul, Korea). Phosphate buffer solution (PBS, pH 7.35) for hemolysis tests was prepared using NaCl (8 g/L), KCl (0.2 g/L), $\text{Na}_2\text{HPO}_4 \cdot 2\text{H}_2\text{O}$ (1.78 g/L) and KH_2PO_4 (0.24 g/L) and sterilized by autoclaving at 1 atm and 121 °C for 15 min. MeB (Methylene Blue - $\text{C}_{16}\text{H}_{18}\text{N}_3\text{ClS} \cdot 3\text{H}_2\text{O}$) was used as model organic dye in photocatalytic activity measurements.

2.1. Synthesis of ZnO and $\text{Zn}_{1-x}\text{Mg}_x\text{O}$ nanoparticles

ZnO and Mg doped ZnO nanoparticles were synthesized by the sol-gel method. In a typical synthesis (Figure 1), methanolic precursor solutions ($\text{Zn}(\text{CH}_3\text{COO})_2 \cdot 2\text{H}_2\text{O}$ and $\text{Mg}(\text{CH}_3\text{COO})_2 \cdot 4\text{H}_2\text{O}$) were prepared with a concentration of 0.25 mol/L. Precursor solutions then aged under magnetic stirring overnight.

To form the gel phase, aging solutions were evaporated at room temperature under magnetic stirring. Then, heat treatment was applied at 400 °C for 10 min to combust the organic residues in the gel phase and at 600 °C for 30 min to obtain an accurate crystal orientation.

2.2. Structural analysis

Phase compositions and crystal structures were characterized by the X-ray diffraction (XRD-Bruker D8 Advance) measurements. Surface morphologies were identified using scanning electron microscopy (SEM-FEI Quanta

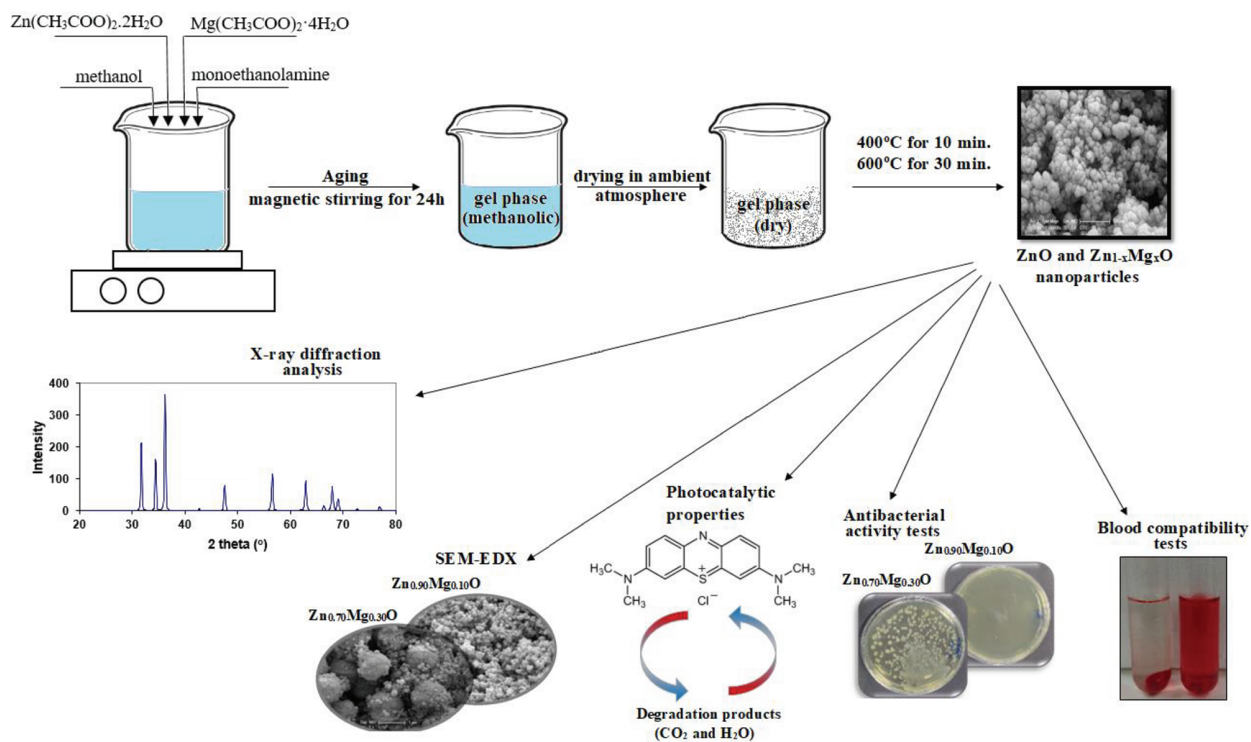


Figure 1. Flow chart for the synthesis and characterization of ZnO and $Zn_{1-x}Mg_xO$ ($x = 0.0, 0.01, 0.02, 0.04, 0.05, 0.10, 0.20,$ and 0.30) nanoparticles.

FEG 250). Energy dispersive X-ray spectroscopy and mapping analysis (SEM-EDX) was used to identify the elemental composition and quantitative concentrations of the constituting elements in nanoparticles.

Nanoparticle suspensions used in the antimicrobial activity tests and hemolytic activity experiments were prepared using DDW and PBS, respectively. Structural stability of suspended nanoparticles in aqueous medium was investigated by determination of Zn and Mg element concentrations in solution phase by the ICP-OES (inductively coupled plasma optical emission spectroscopy – PerkinElmer-Optima 7000 DV, PerkinElmer Corporation, Waltham, MA USA) analysis. Colloidal nanoparticle suspensions in distilled water and the PBS were centrifuged at 2000 rpm for 3 min prior to analysis and supernatant was used. Samples were read after calibrating the ICP-OES device with Zn and Mg standards.

2.3. Evaluation of photocatalytic properties

The photocatalytic performances of ZnO and $Zn_{1-x}Mg_xO$ nanoparticles were investigated by measuring the photocatalytic degradation rate of MeB similar to the procedure given by Ali et al. [64]. Initial dye and nanoparticle concentrations were 1.0×10^{-5} M and 1.0 mg/mL respectively. In a typical photocatalytic degradation experiment, selected samples from Mg doped ZnO nanoparticles and pure ZnO were dispersed in 100 mL of aqueous MeB solution and magnetic stirring was applied for 30 min in the dark to ensure adsorption/desorption equilibrium. Aqueous nanoparticle-MeB dispersions were then irradiated under ambient visible light while being continuously stirred. Also, characteristics of ambient light were examined using CCS200-compact spectrometer and a mixture of light in different wavelengths (436 nm, 546 nm, and 611 nm) were detected.

At appropriate time intervals, constant volume aliquots were taken and then centrifuged at 3000 rpm for 5 min to remove suspended ZnO or Zn_{1-x}Mg_xO nanoparticles. The instant concentrations of MeB were determined using a UV/vis spectrophotometer (Shimadzu UV mini 1240, Shimadzu Corp., Kyoto, Japan) at a wavelength of 664 nm using DDW as reference.

The photocatalytic degradation of MeB followed the first order kinetics and corresponding rate constants were determined by the following equation [65];

$$\ln(A_o/A) = kt,$$

where A_o and A were the absorbances of MeB solution after adsorption equilibrium and after the time (t) respectively. k was the first order rate constant for the photocatalytic degradation. Moreover, the decolorization efficiency of MeB was estimated by the following equation [66];

$$\text{Decolorization (\%)} = (C_o - C/C_o) \times 100,$$

where C_o and C represent the initial concentration of MeB before irradiation, and the concentration of MeB after a certain irradiation time (t), respectively.

2.4. Antibacterial activity tests

Antibacterial activity of Zn_{1-x}Mg_xO NPs was determined by the standard agar plate count method using *E. coli* as model microorganism. Three different concentrations (0.5, 1.0, and 5.0 mg/mL) of ZnO and Zn_{1-x}Mg_xO nanoparticle suspensions were prepared in sterile test tubes by dispersing the NPs in DDW. *Escherichia coli* K12 strain (Invitrogen, France) was used as a model organism in this study. Bacteria were cultivated in tryptic soy broth containing 5 g/L of yeast extract, 10 g/L bactotryptone, and 10 g/L NaCl. After an overnight cultivation at 37 °C, optical density (OD) of bacterial suspension was determined at 600 nm. Then suspension was diluted using fresh tryptic soy broth to final concentration of 1.0×10⁵ cell forming unit(cfu)/mL. 150 µL of this bacterial suspension was inoculated onto each nanoparticle suspension and samples were incubated at 37 °C for 20 h. Test tubes were stirred at 200 rpm under magnetic stirring to keep the contact of NPs and bacteria during incubation period. At the end of incubation time, 50 µL from each test sample was spreaded out onto a TSA plate uniformly, then, plates were incubated at 37 °C for 20 h and the colonies were counted as a final step. Four replicates of each nanoparticle concentration were tested.

2.5. Blood compatibility tests

Human whole blood samples were used in the experiments and hemolytic activity of NPs were investigated according to earlier reports [67]. 4 mL of human blood anticoagulated with trisodium citrate solution (0.108 mM) was added to 10 mL of Ca and Mg free PBS solution and centrifuged at 2000 rpm for 5 min to separate the erythrocytes from plasma. After the supernatant was decanted, RBCs were diluted to 100 mL with PBS. 1.25 mL of this RBC stock solution was added to 5.0 mL of NPs suspensions in test tubes with different concentrations. RBCs suspended in DDW were used as positive control test (100% hemolysis), while RBCs solution dispersed in PBS (pH 7.4) was selected as negative control test (0% hemolysis). All dispersions were incubated under magnetic stirring at 200 rpm at 37 °C for 3 h and then centrifuged at 10,000 g for 3 min using a microcentrifuge. Three replicates of each sample were tested. Hemolysis ratios were calculated by measuring the absorbance value (ABS) of the supernatant solution at 545 nm using a UV-vis spectrophotometer.

3. Results

3.1. Structural analysis

Structural, electrical, magnetic and antibacterial properties of ZnO and ZnO doped with transition metals, strongly depend on the single phase of resulting materials with growth condition. The X-ray diffraction was used to analyze the phase and crystal structure of $\text{Zn}_{1-x}\text{Mg}_x\text{O}$ ($x = 0.0, 0.01, 0.02, 0.04, 0.05, 0.10, 0.20,$ and 0.30) samples synthesized by the sol-gel method which were annealed at $600\text{ }^\circ\text{C}$ in air displayed in Figure 2. The XRD patterns of Mg doped ZnO nanoparticles showed the characteristic peaks of ZnO hexagonal wurtzite structure without secondary phases that for samples having $x \leq 0.20$ concentration, whereas for the higher concentration values an additional MgO phase were observed. The peak (101) was found as the highest peak among all the other indexed peaks (Figure 2).

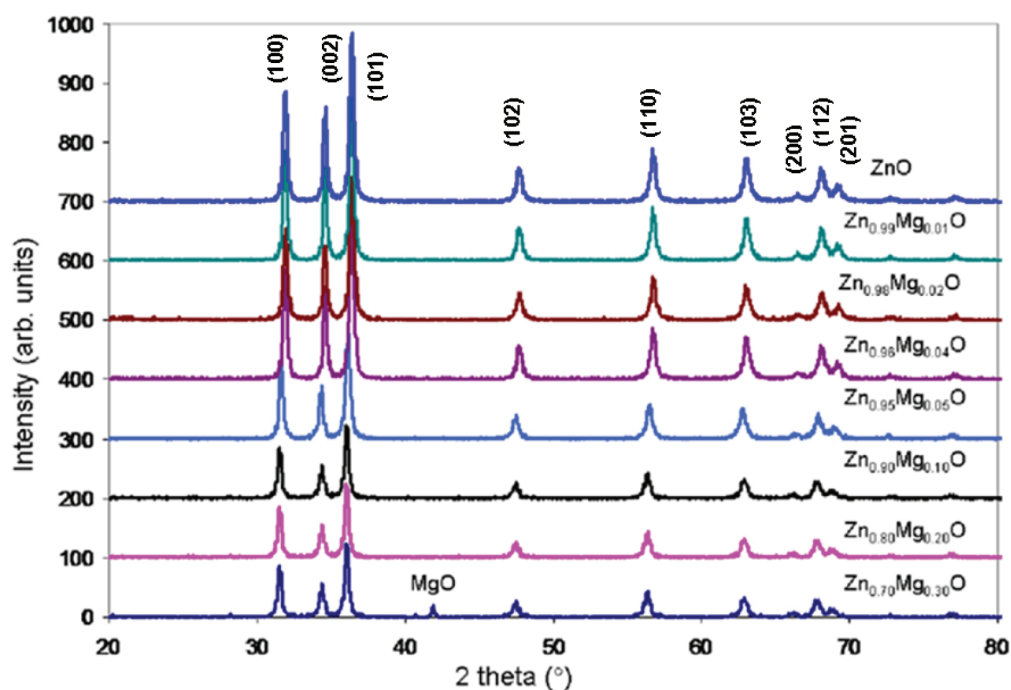


Figure 2. XRD patterns of ZnO and $\text{Zn}_{1-x}\text{Mg}_x\text{O}$ nanoparticles.

$\text{Zn}_{1-x}\text{Mg}_x\text{O}$ ($x = 0.01, 0.02, 0.04, 0.05, 0.10, 0.20,$ and 0.30) nanoparticle, concentration-dependent crystallite sizes (D), lattice parameters (a and c), volume of unit cell, dislocation density (δ) (amount of defect in sample), position and displacement of atoms (u) and bond length (L) were calculated and listed in Table by using XRD analyzes. The detailed evaluations of D , u , V , and L parameters were given below.

The unit cells of $\text{Zn}_{0.99}\text{Mg}_{0.01}\text{O}$ and the crystal structure of $\text{Zn}_{0.99}\text{Mg}_{0.01}\text{O}$ were given in Figure 3. VESTA visualization package was used to illustrate the unit cell of hexagonal Mg doped ZnO as shown in Figure 3a, and randomly 1% Mg-doped to ZnO super cell (Figure 3b) by experimentally obtained parameters which were also displayed in Table.

The average crystallite size was calculated from the XRD peak width of (101) based on the Debye–Scherrer equation [7, 9],

$$D = \frac{K \lambda}{\beta_{hkl} \cos(\theta)} \quad ,$$

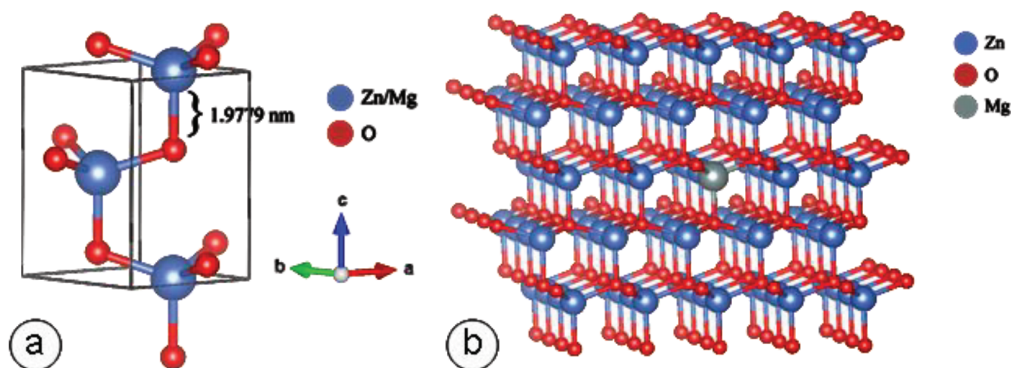


Figure 3. Illustrations of a. the unit cell, and b. the crystal structure of $\text{Zn}_{0.99}\text{Mg}_{0.01}\text{O}$ nanoparticle.

Table . Concentration dependent lattice parameters, atomic packing factor (c/a), crystallite sizes (D), volume of the unit cell, dislocation density (δ) (the amount of defect in the sample), the locality of the atoms and their displacement (u), and bond length (L).

Samples	A(Å)	C(Å)	C/A	D (NM)	Volume V(Å ³)	Dislocation density	U	Bond length (Å)	Microstrain
$\text{Zn}_{0.99}\text{Mg}_{0.01}\text{O}$	3.249	5.210	1.604	26.88	47.629	0.00138	0.3796	1.9779	0.00129
$\text{Zn}_{0.98}\text{Mg}_{0.02}\text{O}$	3.250	5.208	1.602	26.42	47.638	0.00143	0.3798	1.9780	0.00131
$\text{Zn}_{0.96}\text{Mg}_{0.04}\text{O}$	3.250	5.204	1.601	24.2	47.610	0.00171	0.3800	1.9777	0.00143
$\text{Zn}_{0.95}\text{Mg}_{0.05}\text{O}$	3.250	5.202	1.600	23.8	47.597	0.00177	0.3801	1.9775	0.00146
$\text{Zn}_{0.90}\text{Mg}_{0.10}\text{O}$	3.251	5.195	1.598	22.9	47.532	0.00191	0.3805	1.9767	0.00151
$\text{Zn}_{0.80}\text{Mg}_{0.20}\text{O}$	3.251	5.190	1.596	21.8	47.509	0.00210	0.3808	1.9764	0.00159
$\text{Zn}_{0.70}\text{Mg}_{0.30}\text{O}$	3.252	5.182	1.593	21.6	47.468	0.00214	0.3813	1.9759	0.00160

where β_{hkl} is the integral half width, K is a constant equal to 0.90, λ is the wavelength of the incident X-ray ($\lambda = 0.1540$ nm), D is the crystallite size, and θ is the Bragg angle. The particle size calculated for synthesized ZnMgO nanoparticles was in the range of 21.6–26.88 nm.

The lattice constants a and c were calculated with the following formula [7,9]:

$$\frac{1}{d_{hkl}^2} = \frac{4}{3} \left(\frac{h^2 + hk + k^2}{a^2} \right) + \frac{l^2}{c^2}$$

The volume of the unit cell of hexagonal system was calculated by the following equation:

$$V = 0.866xa^2xc$$

ZnO bond length was calculated by the following equation [7,9]:

$$L = \sqrt{\left(\frac{a^2}{3}\right) + [0.5 - u]^2 c^2} \quad ,$$

where a and c are lattice constants of ZnO and u is the wurtzite structure which can be found as

$$u = \left(\frac{a^2}{3c^2}\right) + 0.25 \quad .$$

In a structure, both doping ratio and annealing temperature, are predominantly affecting strain. Therefore, microstrain (ε) was calculated by the following equation:

$$\varepsilon = (\beta_{1/2} \cos\theta) / 4$$

These parameters were presented in Table.

As can be seen from Table, the lattice parameter a and c of the Mg-doped ZnO nanoparticles are in the range of 3.249–3.252 Å and 5.182–5.21 Å, respectively. It was observed that when Mg concentration increased, the lattice parameter a and microstrain increased, and the lattice parameter c and cell volume decreased. There was a reduction in c/a lattice parameter ratio. This was expected since Mg ions replace Zn ions in the lattice, as the Mg (0.59 Å) ions have smaller ionic radii than Zn ions (0.74 Å). Moreover, these results are supported by the low angle shift of XRD peaks, which are correlated with the distortion of the ZnO crystal structure due to the difference of the ionic radius.

As shown in Table, the particle size of the Mg-doped ZnO nanoparticles were in the range of 26.88–21.6. The particle size (D) of the samples decreases with increasing Mg concentration ratio, while the dislocation density (δ) of the samples increases with Mg concentration. This was due to the inverse ratio between δ and D values. The locality of the atoms and their displacements (u parameters) were calculated. It was seen that it was increasing with increasing Mg ratio. The Zn-O bond lengths (L parameters) were in the range of 1.9759–1.9780 Å.

Literature indicated that, reactivity of an element increases as the values of Pauling electro-negativity decrease [68]. Mg is more chemically reactive than Zn, since the Pauling electro-negativity of Mg (1.31) is less than that of Zn (1.65). Thus, Mg can easily be replaced by Zn in the nanoparticle structure. Besides, Mg doping level is expected to change the morphology of ZnO NPs depending on the synthesis method. Mg doped ZnO nanoparticles synthesized via the solution precipitation technique by Iqbal et al. [69] showed a dopant concentration dependent morphology. According to the literature, morphology of $Zn_{1-x}Mg_xO$ NPs may change depending on the synthesis route and this may also cause a significant change on the particles surface area [70,71]. It has also been reported that surface area of NPs decreases with increasing particle size and this causes a decrease in the concentration of ROS generated from nanoparticles [72].

The morphology and element concentrations of Mg doped ZnO NPs were characterized by SEM and EDX, respectively.

Figures 4–11 show SEM micrographs of $Zn_{1-x}Mg_xO$ NPs with varying Mg doping levels i.e. 0%, 1%, 2%, 4%, 5%, 10%, 20%, and 30%. The malting and agglomeration of $Zn_{1-x}Mg_xO$ NPs increase when the concentration of Mg was increased as seen in the figures. From the SEM micrographs, $Zn_{1-x}Mg_xO$ NPs were dense, quasi spherical and agglomerating. At the maximum concentration ($x = 0.30$), as shown in Figure 11, the highest agglomeration and a pellet like dense morphology were observed.

3.2. Photocatalytic measurements

Methylene blue degradation occurs predominantly over the surface of ZnO NPs under the effect of light irradiation [73,74]. Some MeB molecules are adsorbed on the surface of the photocatalyst and the initial MeB concentration equals to the equilibrium concentration of this dye in the solution at the beginning of irradiation time [74]. In our study, adsorption equilibrium of the MeB molecules on the surface of ZnO and $Zn_{1-x}Mg_xO$ nanoparticles was obtained in first 30 min. During this time the solution was kept in dark to avoid photo degradation of MeB.

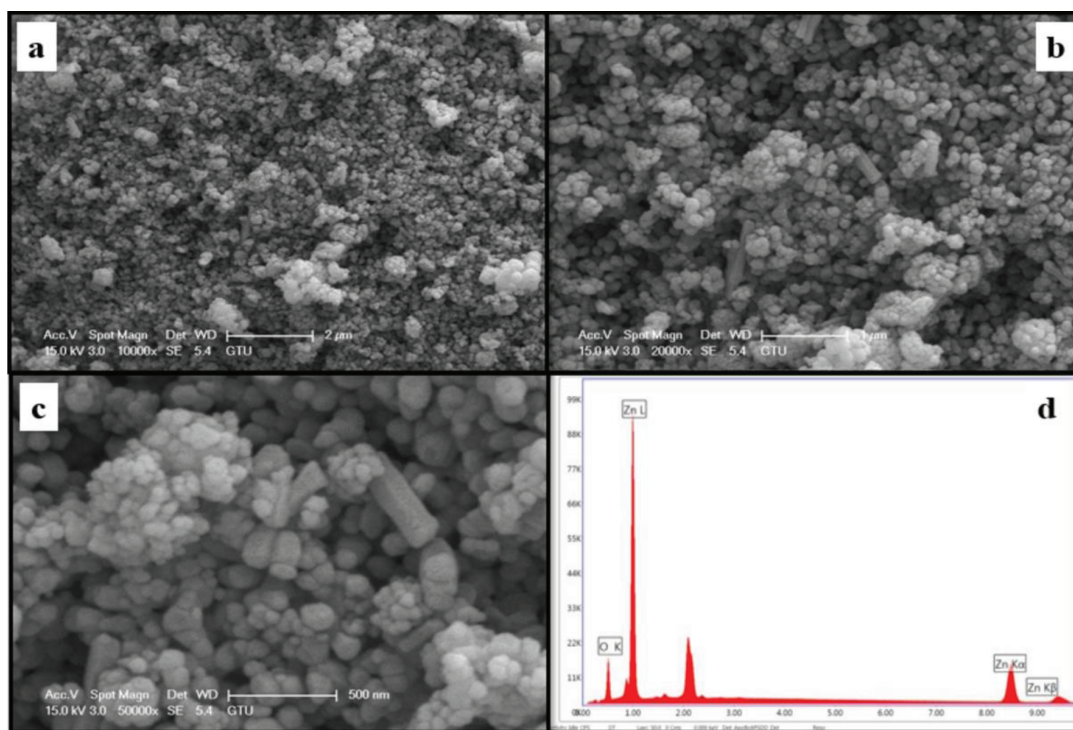


Figure 4. SEM micrographs of ZnO NPs with different magnifications, a. ($\times 10,000$), b. ($\times 20,000$), c. ($\times 50,000$), and d. energy-dispersive X-ray spectrum of ZnO NPs.

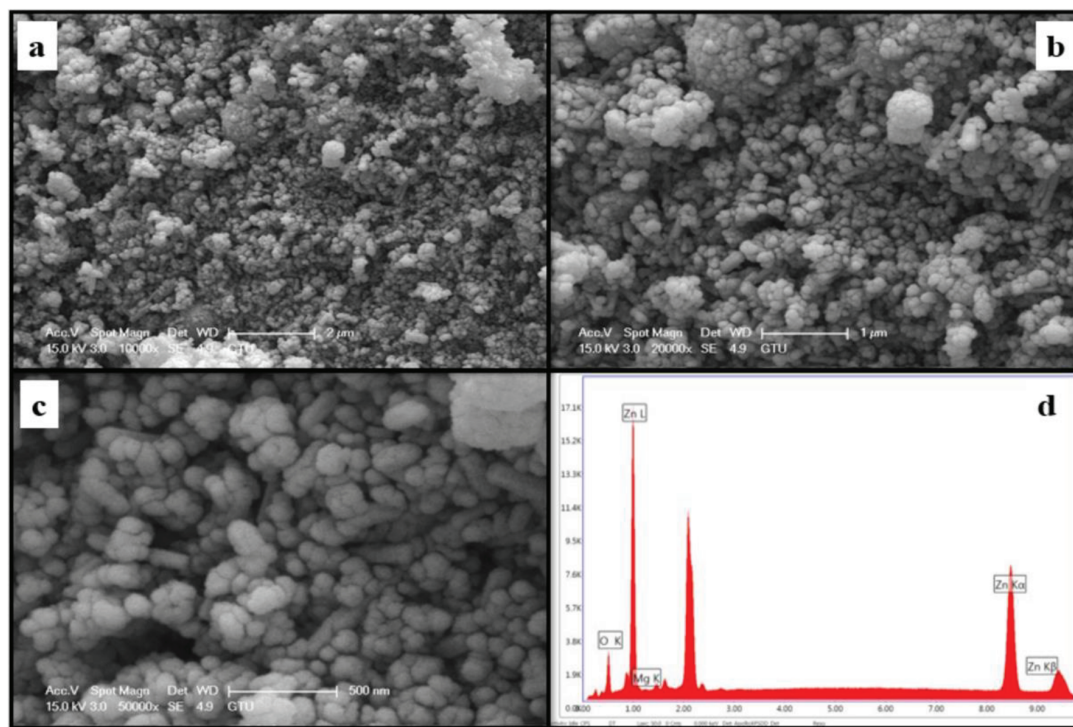


Figure 5. SEM micrographs of Zn_{0.99}Mg_{0.01}O NPs with different magnifications a. ($\times 10,000$), b. ($\times 20,000$), c. ($\times 50,000$), and d. energy-dispersive X-ray spectrum of Zn_{0.99}Mg_{0.01}O NPs.

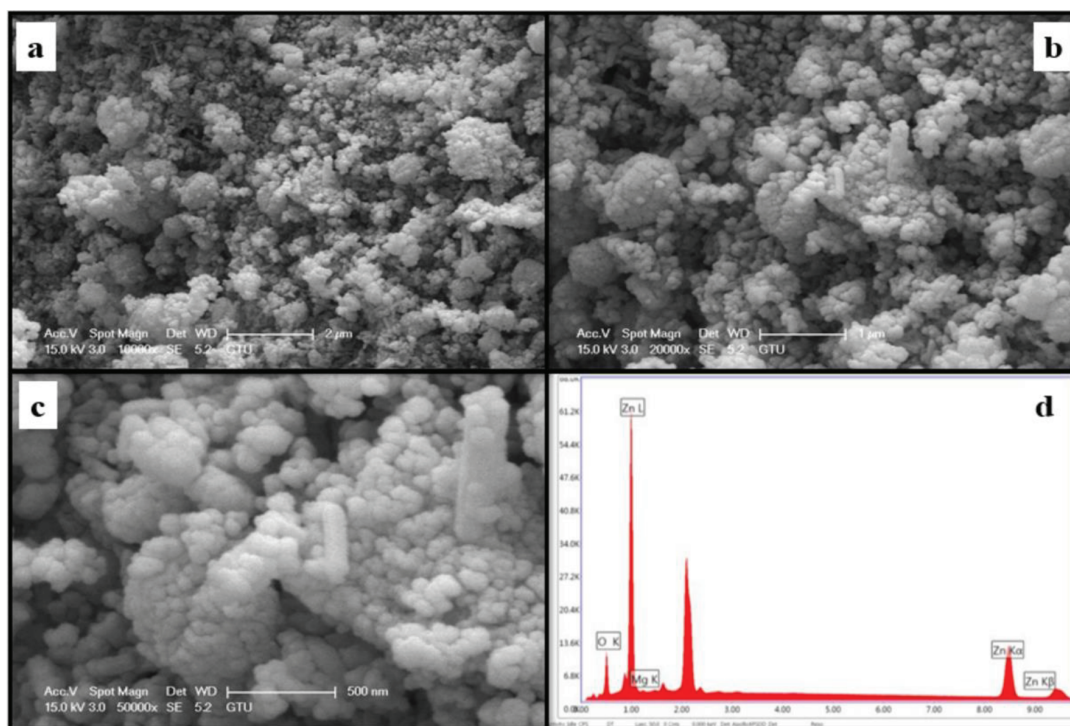


Figure 6. SEM micrographs of Zn_{0.98}Mg_{0.02}O NPs with different magnifications a. ($\times 10,000$), b. ($\times 20,000$), c. ($\times 50,000$), and d. energy-dispersive X-ray spectrum of Zn_{0.98}Mg_{0.02}O NPs.

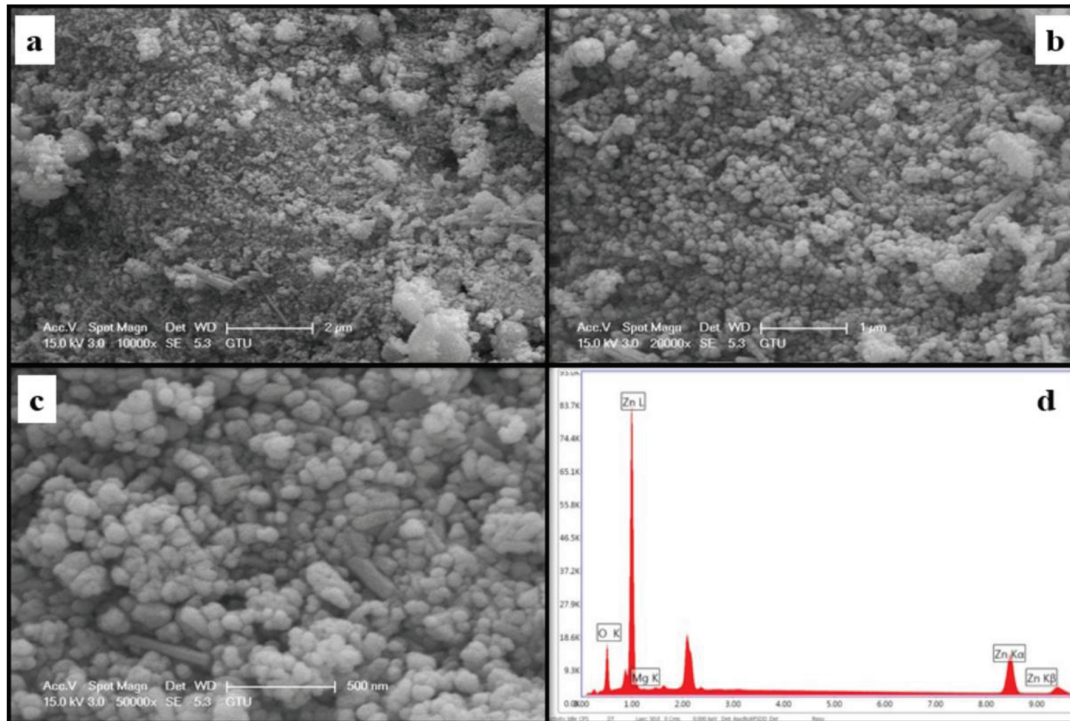


Figure 7. SEM micrographs of Zn_{0.96}Mg_{0.04}O NPs with different magnifications a. ($\times 10,000$), b. ($\times 20,000$), c. ($\times 50,000$), and d. energy-dispersive X-ray spectrum of Zn_{0.96}Mg_{0.04}O NPs.

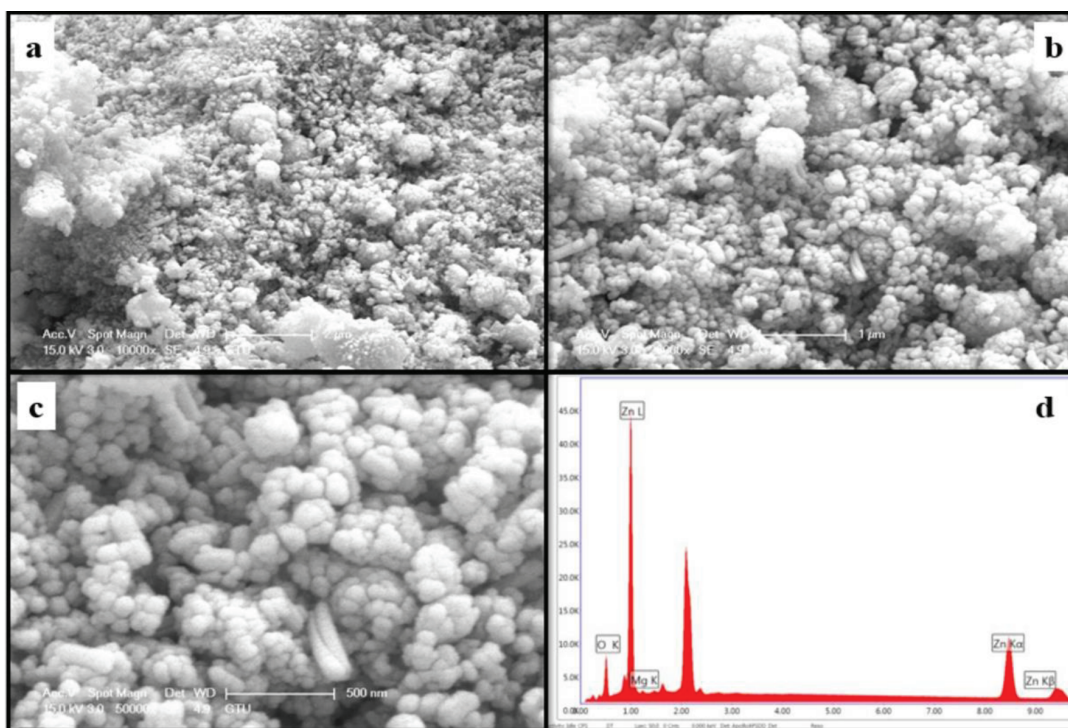


Figure 8. SEM micrographs of Zn_{0.95}Mg_{0.05}O NPs with different magnifications a. ($\times 10,000$), b. ($\times 20,000$), c. ($\times 50,000$), and d. energy-dispersive X-ray spectrum of Zn_{0.95}Mg_{0.05}O NPs.

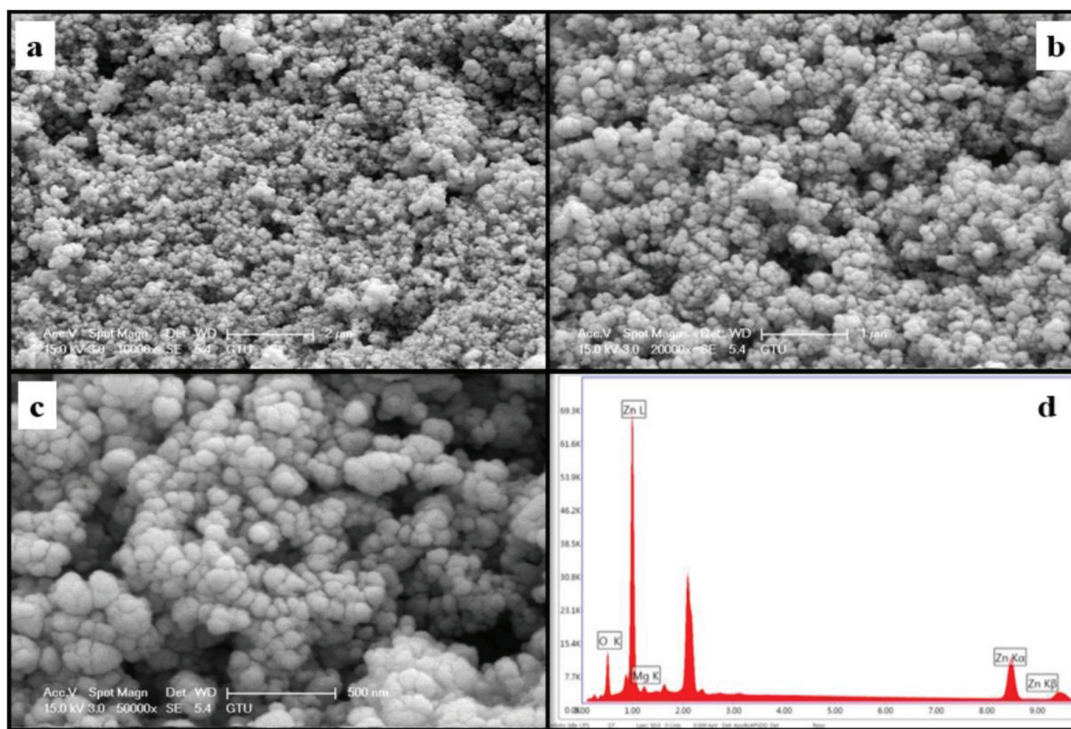


Figure 9. SEM micrographs of Zn_{0.90}Mg_{0.10}O NPs with different magnifications a. ($\times 10,000$), b. ($\times 20,000$), c. ($\times 50,000$), and d. energy-dispersive X-ray spectrum of Zn_{0.90}Mg_{0.10}O NPs.

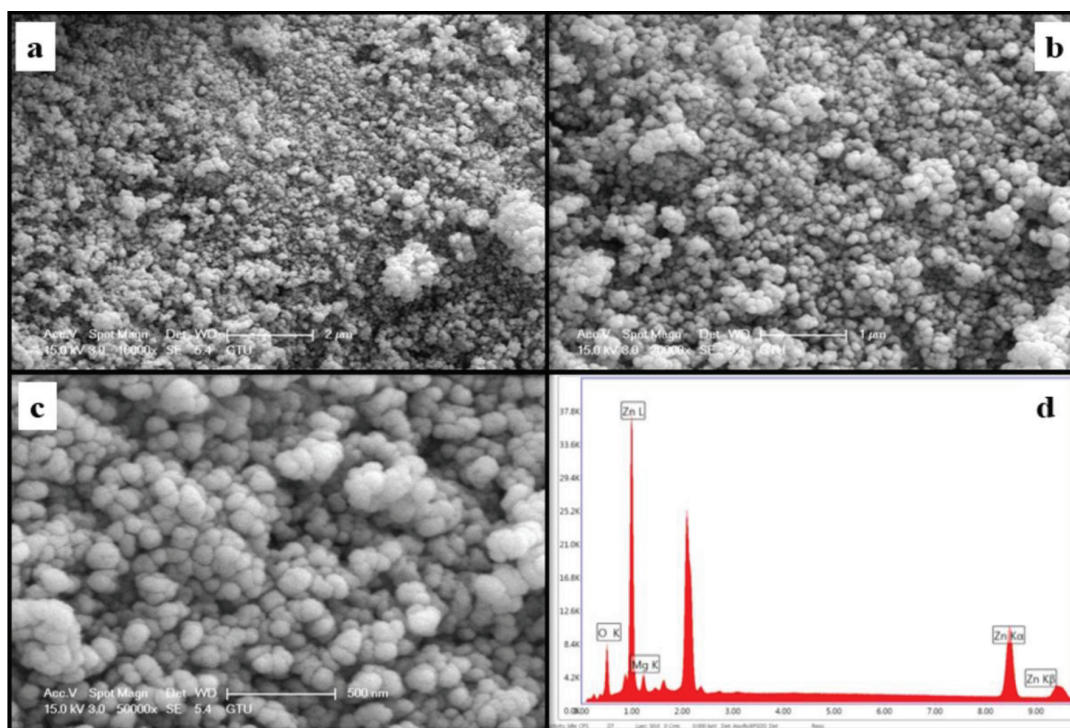


Figure 10. SEM micrographs of $\text{Zn}_{0.80}\text{Mg}_{0.20}\text{O}$ NPs with different magnifications a. ($\times 10,000$), b. ($\times 20,000$), c. ($\times 50,000$), and d. energy-dispersive X-ray spectrum of $\text{Zn}_{0.80}\text{Mg}_{0.20}\text{O}$ NPs.

Figures 12a–12c show the UV-visible absorption spectra of free (unadsorbed) MeB with the variation of time. Attenuation of the intensity of the absorption band at 664 nm indicated the degradation of MeB by both ZnO and $\text{Zn}_{1-x}\text{Mg}_x\text{O}$ photocatalysts. The characteristic band at 664 nm disappeared after 24 h under the effect of ambient light irradiation indicating the complete degradation of MeB by $\text{Zn}_{0.90}\text{Mg}_{0.10}\text{O}$ nanoparticles. Another control experiment was conducted without nanoparticles under same experimental conditions. It was observed that, MeB was not degraded without ZnO or Mg-doped ZnO nanoparticles within 24 h.

The kinetics of MeB photo degradation shown in Figure 12d could be described by a first order kinetics in agreement with the Langmuir-Hinshelwood model:

$$r = -\frac{dC}{dt} = \frac{k_1 k_2 C_o}{1 + k_1 C_o}$$

where k_1 is the adsorption coefficient, k_2 is the specific rate constant for degradation and C_o is the initial concentration of MeB. The integrated form of the above equation can be written as follows:

$$t = \frac{1}{k_1 k_2} \ln \frac{C_o}{C} + \frac{C_o - C}{k_2}$$

If the concentration (C) is very low, then the second term of the equation becomes very small compared to the first one and the equation can be simplified to:

$$\ln \frac{C_o}{C} = k_1 k_2 t \approx k' t$$

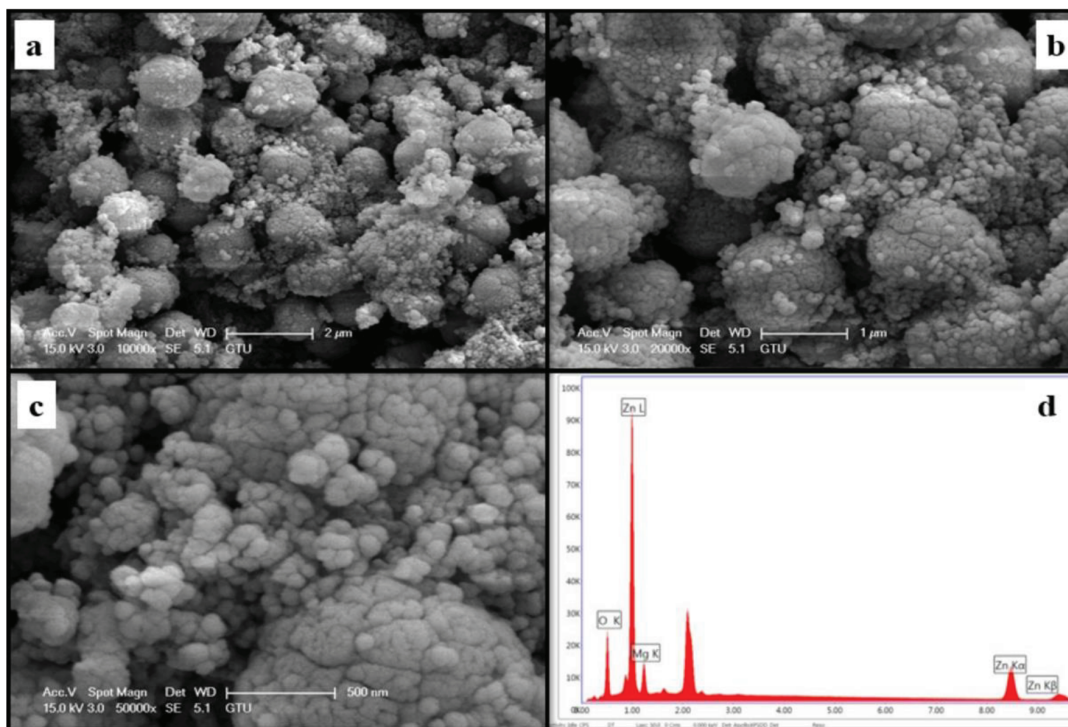


Figure 11. SEM micrographs of $\text{Zn}_{0.70}\text{Mg}_{0.30}\text{O}$ NPs with different magnifications a. ($\times 10,000$), b. ($\times 20,000$), c. ($\times 50,000$), and d. energy-dispersive X-ray spectrum of $\text{Zn}_{0.70}\text{Mg}_{0.30}\text{O}$ NPs.

The plot of $\ln(C_o/C)$ versus irradiation time represents a straight line, whose slope is equal to the apparent first order rate constant (k'). Apparent photodegradation rate constants for undoped ZnO, $\text{Zn}_{0.90}\text{Mg}_{0.10}\text{O}$ and $\text{Zn}_{0.70}\text{Mg}_{0.30}\text{O}$ were 0.0014, 0.0045, and 0.0007 min^{-1} , respectively. Results were consistent with the relevant literature related with MeB degradation [75,76].

Under the effect of electromagnetic radiation (light) the generation of electron-hole pairs between valence bands (VB) and conduction bands (CB) of ZnO NPs are predominantly responsible for the degradation of organic pollutants like MeB via ROS formation [77]. Decolorization of MeB is considered as a demonstrative evidence of its degradation.

ROS formation on the surface of zinc oxide nanoparticles starts with the excitation of electrons in the filled valence band (VB) with electromagnetic radiation having the energy higher than the value of zinc oxides band gap ($\sim 3.3 \text{ eV}$) [78]. Excited electrons are moved to an empty conduction band (CB) to form electron holes in the VB (h_{VB}^+) and free electrons in the CB (e_{CB}^-) (Eq. 1). h_{VB}^+ and e_{CB}^- pairs migrate to the surface of the ZnO nanoparticles and they are involved in redox reactions resulting ROS formation in accordance with the below-mentioned mechanisms [78–81]. While h_{VB}^+ reacts with H_2O molecules in aqueous ZnO suspensions to form OH^* and H^+ , free electrons in the CB react with dissolved O_2 molecules to transform them into superoxide anion radicals (O_2^{*-}) which in turn react with H^+ to generate hydroperoxyl radicals (HO_2^*) (Eqs. 2–4).

To form hydrogen peroxide, hydroperoxyl radicals may collide with each other, or they can also interact with CB electrons and H^+ ions (Eqs. 5–7). H_2O_2 will then react with O_2^{*-} to form OH^* which is a powerful

oxidizing agent (Eq. 8). ROS would be responsible from both antibacterial properties and degradation of organic molecules like MeB into less toxic degradation products such as CO_2 and H_2O (Eq. 9) [53].

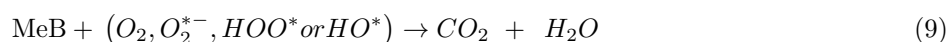
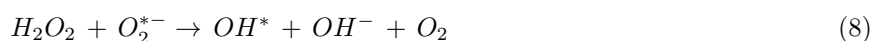
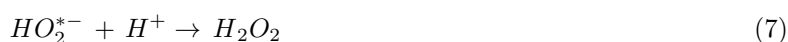


Figure 13 shows the decolorization efficiencies of ZnO, $Zn_{0.90}Mg_{0.10}O$ and $Zn_{0.70}Mg_{0.30}O$ as a function of time. ZnO samples doped by 10% Mg exhibited much higher photocatalytic activity than that of pure ZnO and $Zn_{0.70}Mg_{0.30}O$ nanoparticles. At the end of 1440 min, decolorization efficiency of $Zn_{0.90}Mg_{0.10}O$ was around 99.7% whereas the relevant values for ZnO and $Zn_{0.70}Mg_{0.30}O$ was 87.4% and 66.8% respectively.

3.3. Antibacterial properties

Antibacterial activity of ZnO NPs synthesized by the hydrothermal and the vapor deposition methods is well known in literature [82–85]. Nevertheless, concentration dependent antibacterial activity of ZnO NPs synthesized by the sol-gel method still have unsolved issues.

In this study, activity of $Zn_{1-x}Mg_xO$ NPs against bacteria was examined with different routes. To determine the antibacterial activity of NPs, the Kirby–Bauer disc diffusion method and the agar well diffusion method was first applied. In disc diffusion method, powder form of nanoparticles was pelleted using a hydraulic press, then they were transferred carefully on to the agar plates inoculated with *E. coli*. Similar to the procedure used in the Kirby–Bauer disc diffusion method, the agar plate surfaces were inoculated with the 1×10^6 cfu/mL *E. coli* suspension. Then, a hole for each test sample was punched aseptically with a sterile cork borer, and NPs were placed into wells with three different concentrations in two ways; as solid powder form and as colloidal nanoparticle suspensions in water (30 μ L each). Then, agar plates were incubated at 37 °C for overnight. In both tests, the zone of inhibition could not be formed. As a third route, standard agar plate count method was used.

Antibacterial activities of ZnO and $Zn_{1-x}Mg_xO$ nanoparticles were studied against gram-negative *Escherichia coli* K12 strains. In our study, nanoparticle concentrations were determined as 0.5 mg/mL, 1.0

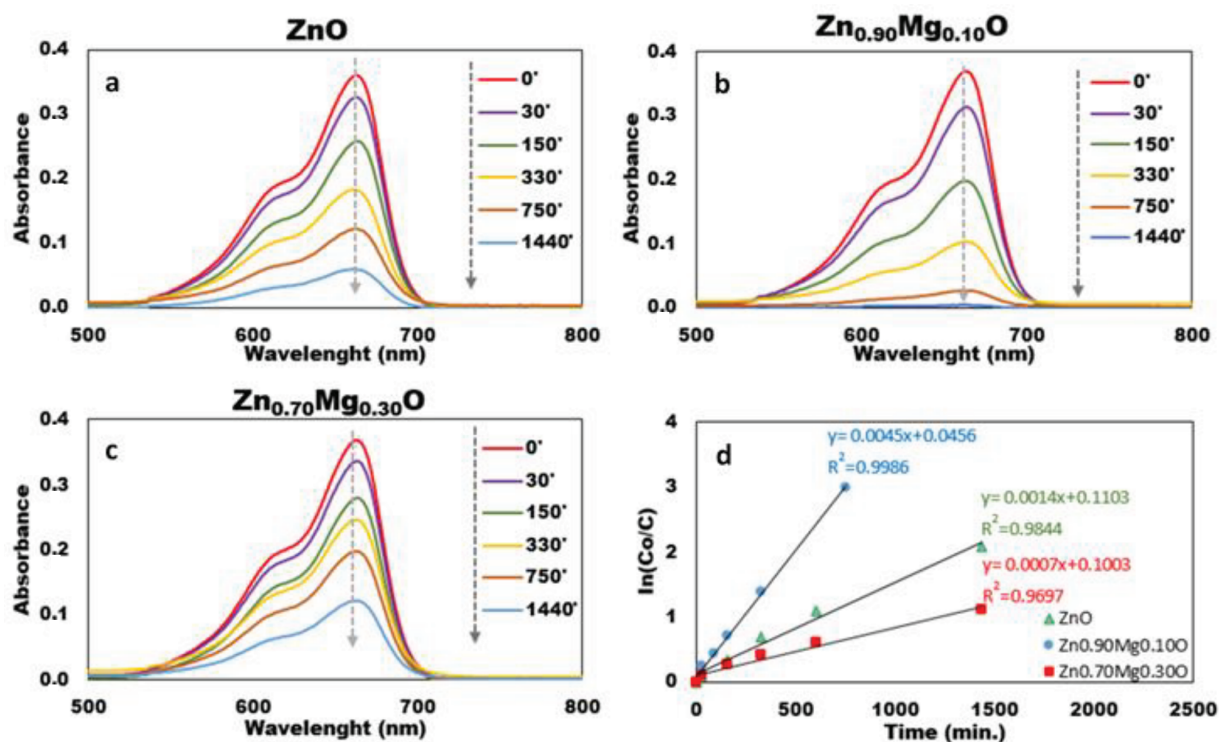


Figure 12. UV-vis spectra of MeB as a function of time in presence of a. ZnO, b. Zn_{0.90}Mg_{0.10}O, and c. Zn_{0.70}Mg_{0.30}O under ambient light irradiation, d. photo degradation kinetics of MeB.

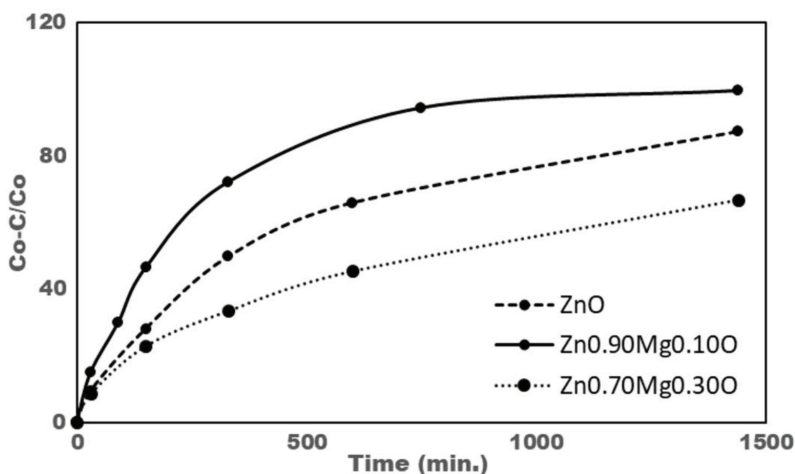


Figure 13. Decolorization efficiencies of ZnO, Zn_{0.90}Mg_{0.10}O and Zn_{0.70}Mg_{0.30}O as a function of time.

mg/mL, and 5.0 mg/mL (corresponding to 6, 12, and 60 mM for ZnO) which was almost 5 times higher than the range reported in the literature [40,85,86]. For undoped ZnO and in low Mg doping levels, antibacterial activity of NPs exhibited both positive and negative concentration dependent behavior (Figure 14). After an overnight incubation period, ZnO NPs showed an antibacterial activity in 0.5 mg/mL and 5.0 mg/mL concentrations. However, at the concentration of 1.0 mg/mL any antibacterial activity was not observed. The same results were obtained for the Zn_{0.99}Mg_{0.01}O sample with lower colony numbers at the same concentration (1.0 mg/mL). In this study, the lowest nanoparticle concentration was 0.5 mg/mL. For ZnO and Zn_{0.99}Mg_{0.01}O,

this lowest concentration may not trigger the defense mechanism of bacteria. As nanoparticle concentration increases antibacterial activity that was observed at low NP concentration disappeared at 1.0 mg/mL. It may be due to some upregulations in bacterial genome as it was stated in literature [87]. Nevertheless, at high ROS concentration due to increased NP concentration (5.0 mg/mL) bacteria could not survive. In a previous study conducted by Khan et al. [88], the effect of type and concentration of ROS on leading to cell death was investigated. Their results proved the varying toxic effects of singlet oxygen, hydroxyl radicals and hydroxyl ions at different concentrations. In another study, effect of $Zn_{0.15}Mg_{0.85}O$ NPs on *Bacillus subtilis* proteome was investigated by controlling the protein profiles by one-dimensional sodium dodecyl sulfate polyacrylamide gel electrophoresis (SDS-PAGE). It was mentioned that, after 5.5 h of exposure to 0.05 mg/mL $Zn_{0.15}Mg_{0.85}O$ NPs, among more than 1550 membrane proteins resolved, the most upregulated ones are related with the toxic metal export (CzcD and CadA), redox conditions and defense (AhpC, BrxA, and BrxB) against ROS [87]. Researchers indicated that bacteria can modify its proteomic structure when they are exposed to harsh environmental conditions.

Mg is an essential element for both prokaryotic and eukaryotic organisms. From $Zn_{0.98}Mg_{0.02}O$ to $Zn_{0.70}Mg_{0.30}O$ (except $Zn_{0.90}Mg_{0.10}O$) due to increasing Mg content, antibacterial activity of nanoparticles weakened at both high and low concentrations (Figure 14).

The reenforcement in the antibacterial activity of $Zn_{0.90}Mg_{0.10}O$ may not be due to the variation in particle size or surface morphology according to SEM-EDX analysis, since our SEM results showed no change in the morphology of nanoparticles. ICP-OES results also proved that ZnO and Mg doped ZnO nanoparticles were quite stable. Presence of Zn^{2+} was not detected in any sample for either pure water or PBS. An insignificant range of 0.145–0.253 $\mu\text{g/L}$ (ppb) was found for Mg^{2+} concentration among all the concentrations of samples. Mg^{2+} levels were very close for all samples, regardless of nanoparticle amount or Mg doping level.

Result indicates that zinc and magnesium in the nanoparticles were not leached in any way and nanoparticles do not dissolve in both water and PBS. Results consistent with XRD analysis (Figure 2) also proved that the nanoparticle structure was not destroyed in pure water and PBS. XRD results indicated a detectable peak corresponded to MgO phase in $Zn_{0.70}Mg_{0.30}O$ sample.

3.4. Blood compatibilities

Nano sized materials may change or deform the morphology of red blood cells (RBCs or erythrocytes) and cause hemolysis, i.e. lysis of cell membrane when they interact with erythrocytes while, ZnO nano particles are regarded as non-toxic, biosafe and possibly biocompatible [28,78]. NPs including ZnO are usually administered intravenously in drug delivery and medical imaging applications [89,90]. However, catalytic activity of the nanoparticle surfaces may cause ROS generation and resulting an increase in oxidative stress leading to cellular damage [53,72,61].

Determination of the hemolytic potential of nanoparticles on human erythrocytes is an alternative method for in vivo testing of biological properties. In a literature study [78], human RBCs were found to be very stable after treatment with 0.100 mg/mL of ZnO NPs (~25 nm in diameter) synthesized by homogeneous gas phase condensation method. In another study, ZnO nanoparticles (~30 nm in diameter) synthesized by solution precipitation method showed no apparent hemolysis up to 0.600 mg/mL [41].

In this study, human erythrocytes drawn from healthy volunteers were used to investigate the hemolytic potentials of ZnO and $Zn_{1-x}Mg_xO$ nanoparticles. Figure 15 shows the hemolysis percentages of blood samples

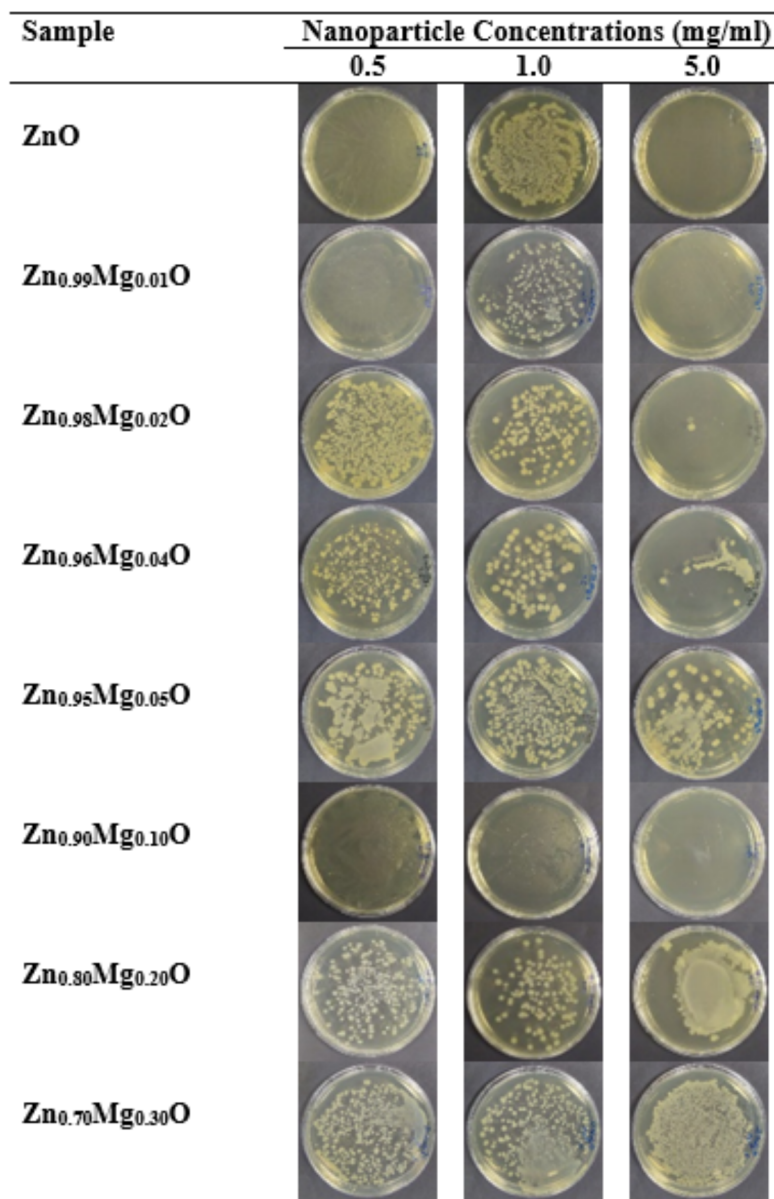


Figure 14. Photographs of agar plate counting method for ZnO and Zn_{1-x}Mg_xO NPs by plate counting. *E. coli* suspensions were treated with different concentrations (0.5, 1.0 and 5.0 mg/mL) of NPs in test tubes for overnight in liquid phase and a small amount of *E. coli* suspension (30µL) treated with NPs from each test tube was inoculated into agar plates. After incubation period, number of colonies in agar plates were observed.

in contact with ZnO and Zn_{1-x}Mg_xO nanoparticles. Results indicated that hemolysis ratio and nanoparticle concentration were directly proportional in case of ZnO and lower than the acceptable level of 5% [91] up to 5.0 mg/mL. In this study, nanoparticle concentrations were 5 times higher compared to the relevant literature [41,85,86].

In the study of Iqbal et al. [92], biocompatibility of cobalt doped ZnO NPs synthesized by coprecipitation method were investigated. They found concentration dependent increments in hemolysis percentages and relatively low hemolysis ratios up to 0.25 mg/mL nanoparticle concentration. In the present study, low

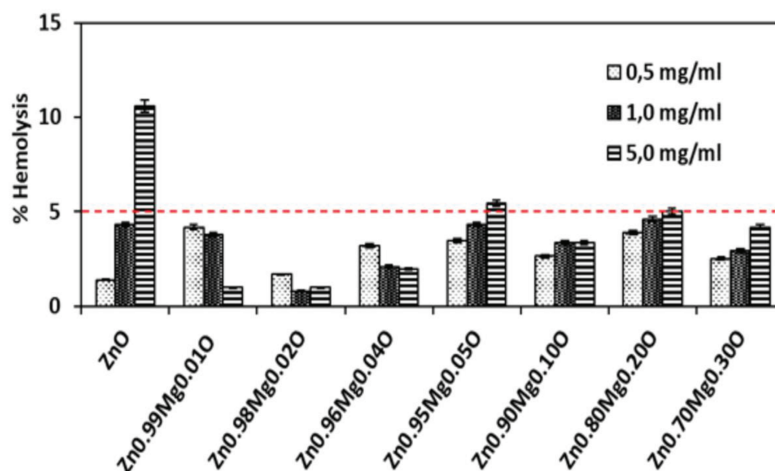


Figure 15. Hemolysis ratios of human erythrocytes after incubation with ZnO and Zn_{1-x}Mg_xO nanoparticles.

hemolytic activity ratios of ZnO and Zn_{1-x}Mg_xO nanoparticles attributed to the homogeneous and highly pure structure of nanoparticles proved by SEM-EDX (Figures 4–11). Also, all Mg doped ZnO nanoparticles (except Zn_{0.90}Mg_{0.10}O at 5.0 mg/mL) showed lower hemolytic activities and hemolysis ratios were concentration dependent for most of the nanoparticles. All Zn_{1-x}Mg_xO nanoparticles indicated much lower hemolytic activities than that of pure ZnO nanoparticles at 5.0 mg/mL. Especially for Zn_{0.90}Mg_{0.10}O sample, both higher antibacterial properties and lower hemolytic ratios were obtained.

4. Conclusion

Pure, chemically and morphologically homogenous, antibacterial and hemocompatible Zn_{1-x}Mg_xO (x = 0.0, 0.01, 0.02, 0.04, 0.05, 0.10, 0.20, and 0.30) nanostructures were successfully synthesized by sol-gel method. Phase composition, antibacterial properties and hemolytic potential of the nanostructured powders were characterized by XRD, SEM-EDX, agar plate counting method and blood compatibility (hemolysis) tests respectively. Results from SEM micrographs demonstrated that Zn_{1-x}Mg_xO NPs were dense, quasi spherical, and agglomerated. An increment was observed in malting and agglomeration of Zn_{1-x}Mg_xO NPs in increased Mg dopant concentration. Additionally, two different phases of ZnO and MgO were obtained, when the Mg concentration was higher than 20%. Zn_{0.90}Mg_{0.10}O and Zn_{0.70}Mg_{0.30}O nanoparticles exhibited better photocatalytic effect on MeB than that of pure ZnO under ambient visible light irradiation. The results of photocatalytic activity tests showed that Zn_{0.90}Mg_{0.10}O exhibited the highest activity, whereas Zn_{0.70}Mg_{0.30}O showed the lowest. The results of blood compatibility tests showed acceptable (<5%) levels [91] of hemolysis ratios for most of our nanoparticle applications. In case of ZnO, hemolysis ratios were below the acceptable level up to 5.0 mg/mL and nanoparticle concentration was also directly proportional to the hemolysis ratios. Additionally, in this study, antibacterial activity of NPs was obtained in both 0.5 mg/mL and 5.0 mg/mL concentrations for ZnO, Zn_{0.99}Mg_{0.01}O and Zn_{0.90}Mg_{0.10}O against *E. coli*. Among these, Zn_{0.90}Mg_{0.10}O showed both higher antibacterial properties and lower hemolytic ratios. As known, in addition to low and/or acceptable hemolytic activity, broad spectrum, high stability, minimum drug resistance and side effects are desired features for antimicrobial drugs. In this respect, Mg doped ZnO nanoparticles and especially Zn_{0.90}Mg_{0.10}O could have commercial applications in UV sterilization systems [93]. The studies and analyses in this study should give valuable ideas

to design and develop new antibacterial nanosized materials for pharmaceutical industry that looking for alternative antibacterial agents in today's world while the effects of classical antibiotics are continuously decreased in recent years.

Acknowledgment

This work was supported by the Scientific Research Project Coordination Center of Bahçeşehir University (BAU) (Scientific Research Project Fund with the Project numbers BAP.2018.02.15 and BAP.2018.02.16).

Conflict of interest

Authors declare that there are no conflicts of interest.

References

1. Zak AK, Majid WHA, Darroudi M, Yousefi R. Synthesis and characterization of ZnO nanoparticles prepared in gelatin media. *Materials Letters* 2011; 65: 70-73.
2. Darroudi M, Ahmad MB, Zak AK, Zamiri R, Hakimi, M. Fabrication and characterization of gelatin stabilized silver nanoparticles under UV-Light. *International Journal of Molecular Sciences* 2011; 12: 6346-6356.
3. Darroudi M, Khorsand Zak A, Muhamad MR, Huang NM, Hakimi M. Green synthesis of colloidal silver nanoparticles by sonochemical method. *Materials Letters* 2012; 66: 117-120.
4. Darroudi M, Sarani M, Kazemi Oskuee R, Khorsand Zak A, Hosseini HA et al. Green synthesis and evaluation of metabolic activity of starch mediated nanoceria. *Ceramics International* 2014; 40: 2041-2045.
5. Edalati K, Shakiba A, Vahdati-Khaki J, Zebarjad SM. Low-temperature hydrothermal synthesis of ZnO nanorods: Effects of zinc salt concentration, various solvents and alkaline mineralizers. *Materials Research Bulletin* 2016; 74: 374-379.
6. Xu H, Wang H, Zhang Y, He W, Zhu M et al. Hydrothermal synthesis of zinc oxide powders with controllable morphology. *Ceramics International* 2004; 30(1): 93-97.
7. Guler A, Arda L, Dogan N, Boyraz C, Ozugurlu E. The annealing effect on microstructure and ESR properties of (Cu/Ni) co-doped ZnO nanoparticles. *Ceramics International* 2019; 45 (2): 1737-1745.
8. Kaya S, Akcan D, Ozturk O, Arda L. Enhanced mechanical properties of yttrium doped ZnO nanoparticles as determined by instrumented indentation technique. *Ceramics International* 2018; 44 (9): 10306-10314.
9. Boyraz C, Dogan N, Arda L. Microstructure and magnetic behavior of (Mg/Ni) co-doped ZnO nanoparticles. *Ceramics International* 2017; 43 (17): 15986-15991.
10. Asikuzun E, Ozturk O, Arda L, Terzioglu C. Microstructural and electrical characterizations of transparent Er-doped ZnO nano thin films prepared by sol-gel process. *Journal of Materials Science-Materials in Electronics* 2017; 28 (19): 14314-14322.
11. Doğan N, Bingölbali A, Arda L. Preparation, structure and magnetic characterization of Ni doped ZnO nanoparticles. *Journal of Magnetism and Magnetic Materials* 2015; 373: 226-230.
12. Claros M, Setka M, Jimenez YP, Vallejos S. AACVD synthesis and characterization of iron and copper oxides modified ZnO structured films. *Nanomaterials* 2020; 10 (3): 471-487.
13. Shaban M, Mohamed F, Abdallah S. Production and characterization of superhydrophobic and antibacterial coated fabrics utilizing ZnO nanocatalyst. *Scientific Reports* 2018; 8 (1): 1-15.
14. Liu J, Ma J, Bao Y, Wang J, Tang H et al. Polyacrylate/surface-modified ZnO nanocomposite as film-forming agent for leather finishing. *International Journal of Polymeric Materials and Polymeric Biomaterials* 2014; 63 (16): 809-814.

15. Sultan SM, Clark OD, Masaud TB, Fang Q, Gunn R et al. Remote plasma enhanced atomic layer deposition of ZnO for thin film electronic applications. *Microelectronic Engineering* 2012; 97: 162-165.
16. Wang ZL. Zinc oxide nanostructures: growth, properties and applications. *Journal of Physics: Condensed Matter* 2004; 16: R829-R858.
17. Patil SL, Pawar SG, Chougule MA, Raut BT, Godse PR et al. Structural, morphological, optical, and electrical properties of PANi-ZnO nanocomposites. *International Journal of Polymeric Materials and Polymeric Biomaterials* 2012; 61 (11): 809-820.
18. Kashyout AB, Soliman HMA, Hassan HS, Abousehly AM. Fabrication of ZnO and ZnO: Sb nanoparticles for gas sensor applications. *Journal of Nanomaterials* 2010; 20: 1-8.
19. Eriksson J, Khranovskyy V, Söderlind F, Käll PO, Yakimova R et al. ZnO nanoparticles or ZnO films: a comparison of the gas sensing capabilities. *Sensors and Actuators B: Chemical* 2009; 137 (1): 94-102.
20. Jońca J, Ryzhikov A, Kahn ML, Fajerweg K, Chaudret B et al. Shape-controlled ZnO nanostructures for gas sensing applications. *Procedia Engineering* 2014; 87: 907-910.
21. Rasmussen JW, Martinez E, Louka P, Wingett DG. Zinc oxide nanoparticles for selective destruction of tumor cells and potential for drug delivery applications. *Expert Opinion on Drug Delivery* 2010; 7 (9): 1063-1077.
22. Sharma H, Kumar K, Choudhary C, Mishra PK, Vaidya B. Development and characterization of metal oxide nanoparticles for the delivery of anticancer drug. *Artificial Cells Nanomedicine and Biotechnology* 2016; 44 (2): 672-679.
23. Li Z, Yang R, Yu M, Bai F, Li C et al. Cellular level biocompatibility and biosafety of ZnO nanowires. *Journal of Physical Chemistry C* 2008; 112 (51): 20114-20117.
24. Mirzaei H, Darroudi M. Zinc oxide nanoparticles: biological synthesis and biomedical applications. *Ceramics International* 2017; 43 (1): 907-914.
25. Fielding G, Bose S. SiO₂ and ZnO dopants in three-dimensionally printed tricalcium phosphate bone tissue engineering scaffolds enhance osteogenesis and angiogenesis in vivo. *Acta Biomaterialia* 2013; 9 (11): 9137-9148.
26. Shruti S, Salinas AJ, Lusvardi G, Malavasi G, Menabue L et al. Mesoporous bioactive scaffolds prepared with cerium-, gallium- and zinc-containing glasses. *Acta Biomaterialia* 2013; 9 (1): 4836-4844.
27. Stoimenov PK, Klinger RL, Marchin GL, Klabunde KJ. Metal oxide nanoparticles as bactericidal agents. *Langmuir* 2002; 18: 6679-6686.
28. Fu G, Vary PS, Lin CT. Anatase TiO₂ nanocomposites for antimicrobial coatings. *Journal of Physical Chemistry B* 2005; 109: 8889-8898.
29. Chiari-Andreo BG, Abucafy MP, Manaia EB, Da Silva BL, Rissi NC et al. Drug delivery using theranostics: an Overview of its use, advantages and safety assessment. *Current Nanoscience* 2020; 16 (1): 3-14.
30. Racca L, Canta M, Dumontel B, Ancona A, Limongi T et al. Zinc oxide nanostructures in biomedicine. *Smart Nanoparticles for Biomedicine* 2018; 171-187.
31. Chmielnicka J, Sowa B. Cadmium interaction with essential metals (Zn, Cu, Fe), metabolism metallothionein, and ceruloplasmin in pregnant rats and fetuses. *Ecotoxicology and Environmental Safety* 1996; 35 (3): 277-281.
32. Petering HG. Some observations on the interaction of zinc, copper, and iron metabolism in lead and cadmium toxicity. *Environmental Health Perspectives* 1978; 25:141-145.
33. Maret W. Zinc in pancreatic islet biology, insulin sensitivity, and diabetes. *Preventive Nutrition and Food Science* 2017; 22 (1):1-8.
34. Soetan KO, Olaiya CO, Oyewole OE. The importance of mineral elements for humans, domestic animals and plants-a review. *African Journal of Food Science* 2010; 4 (5): 200-222.

35. Prasad AS. Biochemistry of zinc. Berlin, Germany: Springer Science & Business Media, 2013.
36. Hu CH, Xia MS. Adsorption and antibacterial effect of copper-exchanged montmorillonite on *Escherichia coli* K88. Applied Clay Science 2006; 31 (3-4): 180-184.
37. Dawlee S, Sugandhi A, Balakrishnan B, Labarre D, Jayakrishnan A. Oxidized chondroitin sulfate-cross-linked gelatin matrixes: a new class of hydrogels. Biomacromolecules 2005; 6 (4): 2040-2048.
38. Jeong H, Hwang J, Lee H, Hammond PT, Choi J et al. In vitro blood cell viability profiling of polymers used in molecular assembly. Scientific Reports 2017; 7 (1): 1-13.
39. Siddiqi KS, Ur Rahman A, Husen A. Properties of zinc oxide nanoparticles and their activity against microbes. Nanoscale Research Letters 2018; 13 (1): 141-154.
40. Zeng K, Li J, Zhang Z, Yan M, Liao Y et al. Lipid-coated ZnO nanoparticles as lymphatic-targeted drug carriers: study on cell-specific toxicity in vitro and lymphatic targeting in vivo. Journal of Materials Chemistry B 2015; 3 (26): 5249-5260.
41. Ågren MS, Chvapil M, Franzén L. Enhancement of re-epithelialization with topical zinc oxide in porcine partial-thickness wounds. Journal of Surgical Research 1991; 50 (2): 101-105.
42. Nieder R, Benbi DK, Reichl FX. Medicinal uses of soil components, geophagia and podoconiosis. Soil Components and Human Health 2018; 35-97.
43. Leslie TA, Greaves MW, Yosipovitch G. Current topical and systemic therapies for itch. Pharmacology of Itch 2015; 337-356.
44. Khaufaire-Uhoda E, Henry F, Pierard-Franchimont C, Piérard GE. Electrometric assessment of the effect of a zinc oxide paste in diaper dermatitis. International Journal of Cosmetic Science 2009; 31(5): 369-374.
45. Zeng H. Blue luminescence of ZnO nanoparticles based on non-equilibrium processes: defect origins and emission controls. Advanced Functional Materials 2010; 20: 561-572.
46. Prasad R, Rattan G. Preparation methods and applications of CuO-CeO₂ catalysts: a short review. Bulletin of Chemical Reaction Engineering & Catalysis 2010; 5: 7-30.
47. Seil JT, Webster TJ. Reduced *Staphylococcus aureus* proliferation and biofilm formation on zinc oxide nanoparticle PVC composite surfaces. Acta Biomaterialia 2011; 7 (6): 2579-2584.
48. Brayner R, Ferrari-Iliou R, Brivois N, Djediat S, Benedetti MF et al. Toxicological impact studies based on *Escherichia coli* bacteria in ultrafine ZnO nanoparticles colloidal medium. Nano Letters 2006; 6: 866-870.
49. Thill A, Zeyons O, Spalla O, Chauvat F, Rose J et al. Cytotoxicity of CeO₂ nanoparticles for *Escherichia coli*. physico-chemical insight of the cytotoxicity mechanism. Environmental Science & Technology 2006; 40: 6151-6156.
50. Reddy KM, Feris K, Bell J, Wingett DG, Hanley C et al. Selective toxicity of zinc oxide nanoparticles to prokaryotic and eukaryotic systems. Applied Physics Letters 2007; 90: 213902-213906.
51. Zhang LL, JiangYH, Ding YL, Povey M, York D. Investigation into the antibacterial behaviour of suspensions of ZnO nanoparticles (ZnO nanofluids). Journal of Nanoparticle Research 2007; 9: 479-489.
52. Kasemets K, Ivask A, Dubourguier HC, Kahru A. Toxicity of nanoparticles of ZnO, CuO and TiO₂ to yeast *Saccharomyces cerevisiae*. Toxicology In Vitro 2009; 23 (6): 1116-1122.
53. Padmavathy N, Vijayaraghavan R. Enhanced bioactivity of ZnO nanoparticles-an antimicrobial study. Science and Technology of Advanced Materials 2008; 9 (3): 035004-035011.
54. Zhang L, Ding Y, Povey M, York D. ZnO nanofluids a potential antibacterial agent. Progress in Natural Science 2008; 18 (8): 939-944.
55. Pati R, Mehta RK, Mohanty S, Padhi A, Sengupta M et al. Topical application of zinc oxide nanoparticles reduces bacterial skin infection in mice and exhibits antibacterial activity by inducing oxidative stress response and cell membrane disintegration in macrophages. Nanomedicine 2014; 10: 1195-1208.

56. Yoshida T. Leaching of zinc oxide in acidic solution. *Materials Transactions* 2003; 44 (12): 2489-2493.
57. Cho WS, Duffin R, Howie SE, Scotton CJ, Wallace WA et al. Progressive severe lung injury by zinc oxide nanoparticles; the role of Zn²⁺ dissolution inside lysosomes. *Particle and Fibre Toxicology* 2011; 8: 27-43.
58. Colvin R, HolmesWR, Fontaine CP, Maret W. Cytosolic zinc buffering and muffling: their role in intracellular zinc homeostasis. *Metallomics* 2010; 2: 306-317.
59. Bisht G, Rayamajhi S. ZnO nanoparticles: a promising anti-cancer agent. *Nanobiomedicine* 2015; 3: 1-11.
60. Gordon T, Perlstein B, Houbara O, Felner I, Banin E et al. Synthesis and characterization of zinc/iron oxide composite nanoparticles and their antibacterial properties. *Colloid Surface A* 2011; 374 (1-3): 1-8.
61. Jalal R, Goharshadi EK, Abareshi M, Moosavi M, Yousefi A et al. ZnO nanofluids: green synthesis, characterization, and antibacterial activity. *Materials Chemistry and Physics* 2010; 121 (1-2): 198-201.
62. Sawai J, Shoji S, Igarashi H, Hashimoto A, Kokugan T et al. Hydrogen peroxide as an antibacterial factor in zinc oxide powder slurry. *Journal of Fermentation and Bioengineering* 1998; 86(5): 521-522.
63. Byamba D, Kim TG, Kim DH, Je JH, Lee MG. The roles of reactive oxygen species produced by contact allergens and irritants in monocyte-derived dendritic cells. *Annals of Dermatology* 2010; 22 (3): 269-278.
64. Ali W, Ulla H, Zada A, Alamgir MK, Muhammad W et al. Effect of calcination temperature on the photoactivities of ZnO/SnO₂ nanocomposites for the degradation of methyl orange. *Materials Chemistry and Physics* 2018; 213: 259-266.
65. Bomila R, Suresh S, Srinivasan S. Synthesis, characterization and comparative studies of dual doped ZnO nanoparticles for photocatalytic applications. *Journal of Materials Science-Materials In Electronics* 2019; 30 (1): 582-592.
66. Phuruangrat A, Aon-on P, Thongtem T, Thongtem S. Synthesis and photocatalysis of Ag₃PO₄ nanoparticles loaded on ZnO nanostructure flowers. *Journal of the Australian Ceramic Society* 2019; 1-6.
67. Yalçın B, Erbil C. Effect of sodium hydroxide solution as polymerization solvent and activator on structural, mechanical and antibacterial properties of PNIPAAm and P (NIPAAm-clay) hydrogels. *Polymer Composites* 2018; 39: E386-E406.
68. Su-Hua Y, Sheng-Yu H, Cheng-Hsun T. Growth mechanisms and characteristics of ZnO nano structures doped with In and Ga. *Japanese Journal of Applied Physics* 2010; 49: 1-8.
69. Iqbal J, Jan T, Ismail M, Ahmad N, Arif A et al. Influence of Mg doping level on morphology, optical, electrical properties and antibacterial activity of ZnO nanostructures. *Ceramics International* 2014; 40 (5): 7487-7493.
70. Stankic S, Suman S, Haque F, Vidic J. Pure and multi metal oxide nanoparticles: synthesis, antibacterial and cytotoxic properties. *Journal of Nanobiotechnology* 2016; 14 (1): 73-93.
71. Sadaiyandi K, Kennedy A, Sagadevan S, Chowdhury ZZ, Johan MRB et al. Influence of Mg doping on ZnO nanoparticles for enhanced photocatalytic evaluation and antibacterial analysis. *Nanoscale Research Letters* 2018; 13: 229-242.
72. Yamamoto O. Influence of particle size on the antibacterial activity of zinc oxide. *International Journal of Inorganic Materials* 2001; 3 (7): 643-646.
73. Saravanan R, Karthikeyan S, Gupta VK, Sekaran G, Narayanan V et al. Enhanced photocatalytic activity of ZnO/CuO nanocomposite for the degradation of textile dye on visible light illumination. *Materials Science and Engineering C* 2013; 33 (1): 91-98.
74. Shen W, Li Z, Wang H, Liu Y, Guo Q et al. Photocatalytic degradation for methylene blue using zinc oxide prepared by codeposition and sol-gel methods. *Journal of Hazardous Materials* 2008; 152 (1): 172-175.
75. Eskizeybek V, Sari F, Gulce H, Gulce A, Avci A. Preparation of the new polyaniline/ZnO nanocomposite and its photocatalytic activity for degradation of methylene blue and malachite green dyes under UV and natural sun lights irradiations. *Applied Catalysis B: Environmental* 2012; 119: 197-206.

76. Yayapao O, Thongtem T, Phuruangrat A, Thongtem S. Sonochemical synthesis of Dy-doped ZnO nanostructures and their photocatalytic properties. *Journal of Alloys and Compounds* 2013; 576: 72-79.
77. Nair MG, Nirmala M, Rekha K, Anukaliani A. Structural, optical, photocatalytic and antibacterial activity of ZnO and Co doped ZnO nanoparticles. *Materials Letters* 2011; 65 (12): 1797-1800.
78. Espitia PJP, Soares NDF, Dos Reis Coimbra JS, De Andrade NJ, Cruz RS et al. Zinc oxide nanoparticles: synthesis, antimicrobial activity and food packaging applications. *Food and Bioprocess Technology* 2012; 5 (5): 1447-1464.
79. Ong CB, Ng LY, Mohammad AW. A review of ZnO nanoparticles as solar photocatalysts: synthesis, mechanisms and applications. *Renewable and Sustainable Energy Reviews* 2018; 81: 536-551.
80. Rajamanickam D, Shanthi M. Photocatalytic degradation of an organic pollutant by zinc oxide – solar process. *Arabian Journal of Chemistry* 2016; 9 (S1): 858-868.
81. Siwińska-Stefańska K, Kubiaka A, Piasecki A, Goscianska J, Nowaczyk G et al. TiO₂-ZnO binary oxide systems: comprehensive characterization and tests of photocatalytic activity. *Materials* 2018; 11 (5): 841-860.
82. Zhu L, Li Y, Zeng W. Hydrothermal synthesis of hierarchical flower-like ZnO nanostructure and its enhanced ethanol gas-sensing properties. *Applied Surface Science* 2018; 427: 281-287.
83. Bazazi S, Arsalani N, Khataee A, Tabrizi AG. Comparison of ball milling-hydrothermal and hydrothermal methods for synthesis of ZnO nanostructures and evaluation of their photocatalytic performance. *Journal of Industrial and Engineering Chemistry* 2018; 62: 265-272.
84. Wasly HS, El-Sadek MA, Henini M. Influence of reaction time and synthesis temperature on the physical properties of ZnO nanoparticles synthesized by the hydrothermal method. *Applied Physics A* 2018; 124 (1): 76-88.
85. Liu Y, He L, Mustapha A, Li H, Hu ZQ et al. Antibacterial activities of zinc oxide nanoparticles against *Escherichia coli* O157: H7. *Journal of Applied Microbiology* 2009; 107 (4): 1193-1201.
86. Shirsekar PP, Kanhe N, Mathe VL, Lahir YK, Dongre PM. Interaction of zinc oxide nanoparticles with human red blood cells. *Bionano Frontier* 2016; 9 (1): 99-104.
87. Auger S, Henry C, Péchoux C, Suman S, Lejal N et al. Exploring multiple effects of Zn 0.15 Mg 0.85 O nanoparticles on *Bacillus subtilis* and macrophages. *Scientific Reports* 2018; 8 (1): 12276-12290.
88. Khan S, Faisal S, Shams DF, Zia M, Nadhman A. Photo-inactivation of bacteria in hospital effluent via thiolated iron-doped nanocerium. *IET Nanobiotechnology* 2019; 13 (8): 875-879.
89. Fujihara J, Tongu M, Hashimoto H, Yamada T, Kimura-Kataoka K et al. Distribution and toxicity evaluation of ZnO dispersion nanoparticles in single intravenously exposed mice. *The Journal of Medical Investigation* 2015; 62 (1.2): 45-50.
90. Tongu M, Hashimoto H, Yamada T, Kimura-Kataoka K, Yasuda T et al. Comparison of acute toxicity of ZnO and silica-coated ZnO nanoparticles in mice after single intravenous injection: preliminary experiment to apply to biological imaging. *Shimane. Journal of Medical Science* 2014; 31: 7-11.
91. Ma D, Tu K, Zhang LM. Bioactive supramolecular hydrogel with controlled dual drug release characteristics. *Biomacromolecules* 2010; 11 (9): 2204-2212.
92. Iqbal G, Faisal S, Khan S, Shams DF, Nadhman A. Photo-inactivation and efflux pump inhibition of methicillin resistant *Staphylococcus aureus* using thiolated cobalt doped ZnO nanoparticles. *Journal of Photochemistry and Photobiology B: Biology* 2019; 192: 141-146.
93. Romo LF, Cinoglu A, Moses D. 2019; U.S. Patent Application No. 16/454,385.